Vortical Flow Effects on Flow Separation Control

By

Yangliu Liu

Submitted to the graduate degree program in Aerospace Engineering and the Graduate Faculty of the University of Kansas in partial fulfillment of the requirements for the degree of Master of Science.

_____

Chairperson Zhongquan Zheng

_____

Ray Taghavi

_____

ZJ Wang

Date Defended: 06 June 2016

The Thesis Committee for Yangliu Liu
certifies that this is the approved version of the following thesis:

Vortical Flow Effects on Flow Separation Control

_____
Chairperson Zhongquan Zheng

Date approved: 06 June 2016

Abstract

The effect of Reynolds number, oscillation frequency, amplitude, and the incident angle on flow separation control is studied numerically in this thesis. Two configurations are investigated, cylinders in tandem and the cylinder-airfoil arrangement. The upstream cylinder changes locations, size, and oscillating frequencies and amplitudes, which necessitates investigating its effect on separation control of the downstream cylinder or airfoil. A validation simulation based on an airfoil in the wake of a stationary cylinder is carried out to verify the numerical method that will be used in this study.

The results show that high-Reynolds-number, high-frequency low-amplitude oscillation motion of the upstream cylinder reduces the flow separation on the downstream airfoil. By placing an oscillating cylinder in the upstream, the flow separation point moves slightly further downstream even at zero angles of attack.

Acknowledgments

I would like to thank my advisor, Dr. Zhongquan Charlie Zheng, without whom this work would not have been possible. Dr. Zheng is not only my advisor in study, but also my advisor in life. He introduced me to the world of fluid dynamics.

Special thanks should be given to my classmate and friend Meihua Zhang, who helped me with coding.

Finally, I would like to give the most special thanks and much love to my parents, who provided me the chance to study abroad at the University of Kansas and supported me throughout my journey.

Table of Contents

List of Figures

List of Tables

1 INTRODUCTION

The effects of an upstream object on flow behaviors around the downstream object are of interest in many fluid dynamic applications. By understanding the mechanisms of flow interactions between the two objects, these effects can be used for flow control purposes. In this study, flow behaviors around two tandem cylinders and cylinder-airfoil configurations are studied numerically to investigate the effect on flow separation of the downstream object.

The viscous flow past a bluff body has received significant interest and been well-studied in the past few decades, especially in the field of the flow around a circular cylinder. The understanding of the flow behaviors around the cylinder includes the boundary layer, the wake, and the dynamics of the vortices. Therefore, most of the experimental and numerical research has focused on the flow around a circular cylinder or an airfoil. Flow separation occurs when it past a bluff body, which can result in increased drag and reduced lift. Therefore, a variety of researches have gone into the design that can reduce or delay the flow separation and keep the local flow attached for as long as possible. Control methods include using actuators, vortex generators, canard, and dimples on the surface. Among these methods, using an oscillating cylinder in the upstream of a bluff body to control flow separation evokes the current research interests.

However, the flow past two or more bluff bodies, such as circular cylinders in an array or cylinder-airfoil configuration, has received less attention. Despite that, studies on the topic still contain interesting phenomena of the flow around, behind, and between the cylinders.

Common sense dictates that different arrangements will affect the results. In previous studies, due to the diverse purpose of research, cylinders have been arranged in a variety of forms. The most commonly and widely used configurations are in-line, tandem, and complex arrays. In order to understand the characteristics of multi-cylinder arrangements, this

fundamental study focuses on the flow over two cylinders in side-by-side, or tandem, and staggered configurations.

Many pioneers—such as Borazjnai and Sotiropoulous[1]; Papaioannou et al.[2]; Lai et al.[3]; Tu et al.[4]; Gu and Sun[5]; Igarashi[6]; Kang[7]; Dalton et al.[8]; Xu et al.[9]; Zhou et al.[10]; Summer et al.[11]; Keser and Unal[12]; Zhou et al.[13]; Lin et al.[14]; Deng et al.[15]; Meneghini et al.[16]; Kitagawa and Ohta[17]; Carmo and Meneghini[18]; Mahir and Rockwell[19]; Yang and Zheng[20]; Li et al.[21]; Sharman et al.[22]; Bao et al.[23]; and Zdravkovich[24]; —have done significant work, mostly on the flow past stationary or multiple cylinders, and flow-induced vibration of cylinders. Other researchers—including Toebes[25]; Griffin[26]; Tanida et al.[27]; Griffin and Ramberg[28]; King[29]; Durgin et al.[30]; Williamson and Roshko[31]; Oliger and Sreenivasan[32]; Ongoren and Rockwell[33]; Mittal and Kumar[34]; and Blackburn and Henderson[35]—have studied the flow past a cylinder with forced oscillations.

The characteristic of flow over cylinder-airfoil configuration is also one of the most interesting topics of flow past two or more bluff bodies. Researchers such as Sturm et al.[36]; Jiang et al.[37]; Bouzaher[38]; Liao et al.[39]; Takagi et al.[40]; Wei et al.[41]; have studied the characteristics of the flow over an airfoil in the wake of the upstream cylinder.

In cases examining the flow past two cylinders, the configurations, as mentioned previously, typically are tandem (in-line), side-by-side (cross-flow), or staggered.

Papaioannou et al.[2] investigated the flow past two oscillating cylinders using numerical simulation. At a low Reynolds number, the two tandem cylinders oscillated under the same amplitude and frequency with either the same or opposite phase to investigate the lock-in regions in the diagrams of amplitude versus frequency. The spacing ratio and the Reynolds number are the key parameters that will determine the wake flows. For the stationary situations, the spacing ratio L/D (L is the center-to-center distance of two cylinders, and D is the diameter of the

cylinder) is between 3.5 and 4.0, in which the type of flow interference changes in the laminar region[2]. At a smaller spacing ratio, the two cylinders act like a single object, and the vortices only occur in the wake of the downstream cylinder. There is a critical spacing distance below which vortex formation from the upstream cylinder cannot be fully accomplished, as shown in Yang and Zheng[20], Li et al.[21] and Sharman et al.[22]. When the spacing ratio is above a critical level, say 4.0, vortex shedding can be found between the two cylinders. This critical spacing is marked by a sudden jump in the Strouhal number of the flow system.

In Mittal et al.'s[34] study, the spacing ratio between two cylinders was as large as 5.5*D* (*D* is the cylinder diameter). Mittal et al. concluded that the performance of the upstream cylinder was similar to an isolated one, while the downstream cylinder showed significantly large amplitude in the transverse direction. This was because the downstream cylinder is in the upstream cylinder's well-developed vortices shed as the spacing ratio is large, giving rise to its stronger oscillations. Bao et al.[23] studied two cylinders with a spacing ratio of 5.0. The researchers also indicated that the front cylinder acted like a single cylinder, but the rear cylinder was greatly affected by the upstream wake.

Kang[7] numerically simulated two side-by-side cylinder configurations at a low Reynolds number. The wake pattern, lift, and drag distribution were investigated and compared with both experimental and numerical results. Kang indicated that two non-dimensional flow parameters affecting the flow between two cylinders were Reynolds number and the spacing ratio between cylinders. Kang also highlighted that, when the spacing ratio was equal or greater than 5, the mutual interference between two wakes disappeared, leading two single cylinder cases. By simulating two cylinders in a side-by-side arrangement, Kang concluded that the mean lift and drag coefficients were mainly dependent on the spacing ratio and were relatively insensitive to

the Reynolds number, whereas the flow fluctuation depended strongly on both the spacing ratio and Reynolds number.

The oscillations of the cylinders significantly affected the flow. In certain cases, the motion of the cylinder led to vortex shedding that differs significantly from the shedding usually observed for flow past a stationary cylinder.

Zdravkovich[24] indicated that the fluid dynamic interactions between two stationary cylinders were quite sensitive to their relative arrangement. Similar conclusions were drawn as well; if the cylinders were far apart, the flow around either of them was similar to that of a single cylinder. In addition, Zdravkovich[24] classified three types of the interference of the two cylinders if they were close or the back cylinder was in the wake of the front one: proximity interference, wake interference, and proximity and wake interference. Proximity interference is usually seen for transverse and closely spaced cylinder arrangements. Two cylinders affect the formation of both vortex streets in this type. Wake interference is commonly seen for two cylinders in tandem and staggered arrangements when the spacing ratio between two cylinders is sufficiently large. The upstream cylinder is unaffected by the presence of the downstream one. However, the downstream cylinder lies in the wake of the upstream cylinder and suffers interference effects. When the two cylinders are close, both of them affect the flow past each other.

In order to study the effect on the downstream cylinder, experiments employing forced transverse vibration have been carried out. In some of the studies involving forced oscillating cylinders, the upstream cylinder was fixed and allowed the downstream one to oscillate only in the transverse direction.

As extensively studied in the work of Williamson and Roshko[31], it is known that, for large amplitudes—which means the amplitude is greater than about half a cylinder diameter—the mode of vortex shedding is not always the same as that described by the von Karman vortex street model.

Besides flow past cylinders, flow past an airfoil with a cylinder in front of it has also been well-studied. Wei et al.[41] studied flow separation behavior of a stationary single hydrofoil at a low Reynolds number. The NACA634-021 profile was used in their study. By changing the inflection angles, some phenomena were carried out of flow separation. The angles of attack were 0°, 10°, 15°, and 20°. The researchers pointed out that obvious flow separation could be detected even at a0° angle of attack. As the angle of attack increased, the flow had already separated at the leading edge. For larger angles, such as 15° and 20°, very evident recirculating flow could be observed. Wei et al. [41] indicated that at 0° incident angle, the flow separated from the hydrofoil surface at about half chord length and formed a small flow recirculating bubble. When the angle was increased to 10°, a significant flow recirculating bubble was generated. When the angle increased to 15°and 20°, a large flow recirculation region could be observed. The researchers also indicated that the flow tended to reattach to the hydrofoil surface once separated flow was produced. As soon as the flow separated from the leading edge, it reattached to the hydrofoil surface. Further, there was a critical point in the streamlines when the angle was 15°. Also, when the angle increased, the flow separation became unstable. [41]

Liao et al.[39] numerically studied the vortex formation and force characteristics of the airfoil in the wake of a circular cylinder. Three parameters affected the configuration: the spacing between two objects, the transverse distance, and the incident angle of the airfoil. The airfoil in their study was chosen as an elliptical shape. By studying the averaged lift and drag

coefficient characteristic of the airfoil at a different position, the researchers concluded that both time-averaged lift and drag coefficient decreased as the transverse distance increased till zero distance, and then both C_D and C_L increased as the transverse distance increased. For averaged lift and drag coefficient versus spacing, however, the trend was totally different. Both C_D and C_L first increased, then decreased as the spacing increased. Last, for different incident angles, both averaged lift and drag coefficient were proportionate to the incident angle when the angle was small. A validation simulation for Liao et al.'s results will be carried out later in this paper.

Besides Liao et al.[39], Takagi et al.[40] studied the aerodynamic characteristics of the NACA0018 airfoil in the wake of the cylinder at a high Reynolds number. The configurations in their study were in-line and staggered. Though the Reynolds number was much larger than that in the Liao et al. paper, similar results were achieved in time-averaged lift and drag coefficient versus incident angle. Takagi et al. indicated that the time-averaged drag coefficient was proportional to the incident angle for both cases with a cylinder and those without cylinder. The averaged C_L decreased at a relatively large angle of attack, which was due to the influence of the upstream cylinder wake. The researchers also indicated that the pressure coefficient was influenced by the wake of the cylinder, too. Due to the upstream cylinder, the pressure coefficient of the suction surface was smaller than that without a cylinder, while the pressure distribution on the pressure surface increased. By comparing the pressure distribution and vorticity contour with that of without the cylinder wake, the flow separation was reduced and controlled by the cylinder wake.

Bouzaher[38] studied the numerical simulation of the flow around a NACA2415 airfoil at an 18° angle of attack at a low Reynolds number, the flow separation control effect, and the force characteristics of the airfoil by using a rod in front of it. When the angle of attack increased, the

separation and the transition points moved toward the leading edge. Flow control through the boundary layer could reduce the drag, enhance the lift, and improve the performance of the aircraft.

In this paper, in Section 2, simulations on tandem cylinders and cylinder-airfoil configurations using the numerical method are carried out. In order to verify the numerical method, a validation simulation based on Liao et al.'s study is carried out in Section 3. The results and discussion are presented in Section 4. Finally, the conclusions based on the results are classified in Section 5.

2 SIMULATION TOOL AND METHOD

2.1 Simulation Tool

In this paper, numerical simulation is implemented using the software ANSYS 15[42]. The two configurations are the tandem-cylinder and cylinder-airfoil setups. In both configurations, the upstream cylinder changes locations, size, and oscillating frequencies and amplitudes, which requires investigating the effect on separation control of the downstream cylinder or airfoil. The description of the model is presented in the next section, followed by the results and conclusions.

2.2 Simulation Method and Configurations

The configurations of the models are shown in Figure 1, with (a) for the cylinder-cylinder configuration and (b) for the cylinder-airfoil configuration. In the tandem-cylinders configuration, the diameters of upstream and downstream cylinders are $0.3D$ and $1D$, respectively. In the cylinder-airfoil configuration, the airfoil is chosen as the NACA0015 shape with $1D$ chord length. The upstream cylinder diameter is $0.1D$ in cylinder-airfoil cases.

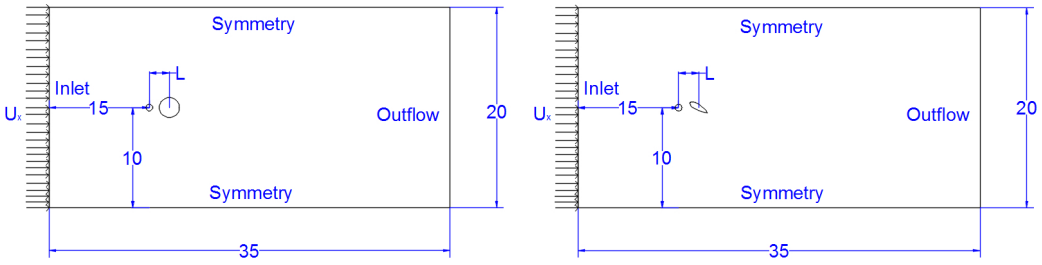

(a) (b)

Figure 1 Sketch of the configurations for simulation and the boundary conditions: (a) tandem cylinders, (b) cylinder-airfoil configuration.

The simulation is carried out using the ANSYS 15[42] software to simulate the two-dimensional, unsteady, incompressible flow.

The unsteady incompressible Navier-Stokes equations in their non-dimensional form can be written as

$$\frac{\partial \boldsymbol{q}}{\partial t} + \boldsymbol{q} \cdot \nabla \boldsymbol{q} - \frac{1}{Re} \nabla^2 \boldsymbol{q} + \nabla p = f \quad (1)$$

and

$$\nabla \cdot \boldsymbol{q} = 0 \ . \quad (2)$$

The relative contributions of convection and diffusion are defined by the Reynolds number:

$$Re = \frac{U_\infty D}{\nu} \ , \quad (3)$$

where D denotes the downstream cylinder diameter or airfoil chord length, U_∞ is the incoming velocity, and ν is the kinematic viscosity of the fluid.

The scheme is selected as first-order in time and second-order upwind in space. Both laminar and turbulent flow cases are considered according to different Reynolds numbers of the flow. The Reynolds number is defined in Eq.(3). For both laminar and turbulent cases, the laminar model is used for simulation. In this paper, the Reynolds numbers are 500, 2500, and 10000.

The oscillation motion of the front cylinder is specified as a harmonic sinusoidal oscillation in the cross-flow direction:

$$y(t) = A \sin(2\pi f t) \ , \quad (4)$$

where A and f are the oscillation amplitude and frequency, respectively. The amplitudes are tested at 1/16, 1/8, and 1/4 of D. The frequencies are 2, 4, and 8[37]. The mesh around the

upstream cylinder oscillates with the cylinder using the unstructured dynamic mesh function in ANSYS 15[42].

The unstructured mesh layouts of the entire domains for both tandem-cylinders and cylinder-airfoil configurations are shown in Figure 2. The maximum mesh size for boundaries is 1*D*. In tandem-cylinders configurations, there are 60 and 180 nodes for the upstream and downstream cylinders, respectively. In cylinder-airfoil configuration, 30 and 180 nodes are used for cylinder and airfoil, respectively. The detailed mesh layouts around tandem-cylinders and cylinder-airfoil configurations are shown in Figure 3 and Figure 4, respectively.

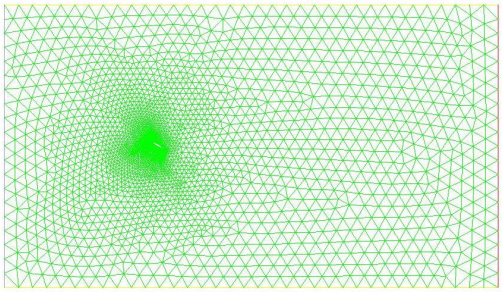

Figure 2 Mesh of simulation domain.

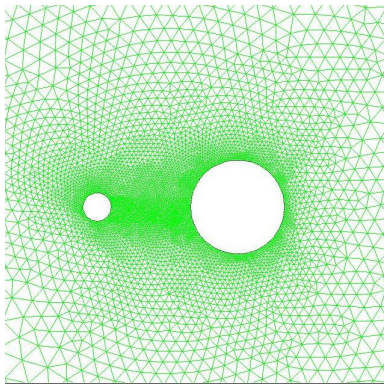

Figure 3 Mesh layout of tandem-cylinders configuration.

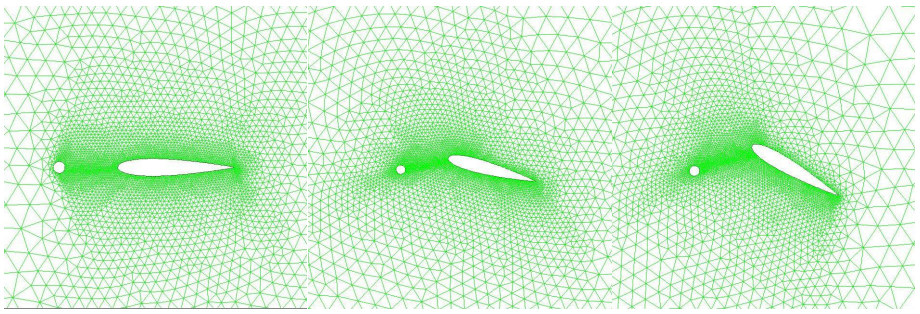

(a) (b) (c)

Figure 4 Detailed meshes of cylinder-airfoil configurations at different incident angles: (a) 0°, (b) 15°, and (c) 30 °.

3 VALIDATION SIMULATION

In this section, a validation simulation is carried out based on Liao et al.'s[39] study on cylinder-airfoil configuration.

3.1 Configuration and Simulation Tool

As discussed in Section 1.2, Liao et al.[39] showed that the three parameters affecting the flow around the airfoil were incident angle, spacing ratio, and transverse distance. Their study was simulated under a low Reynolds number, Re=500. The configuration of the simulation is shown in Figure 5. The domain is a 30D height 45D weight rectangular, where D is the cylinder diameter and airfoil chord length. The cylinder is placed on the centerline of the domain, where L_{inlet}=15D. In addition, the elliptical-shaped airfoil is in the downstream of the cylinder. The spacing L and transverse distance d are determined by different cases, as shown in Table 1. The Reynolds number in this simulation is defined as $U_\infty D/v$, where U_∞ is the incoming flow velocity, D is the diameter cylinder or the chord length of the airfoil, and v is the kinematic viscosity of the fluid.

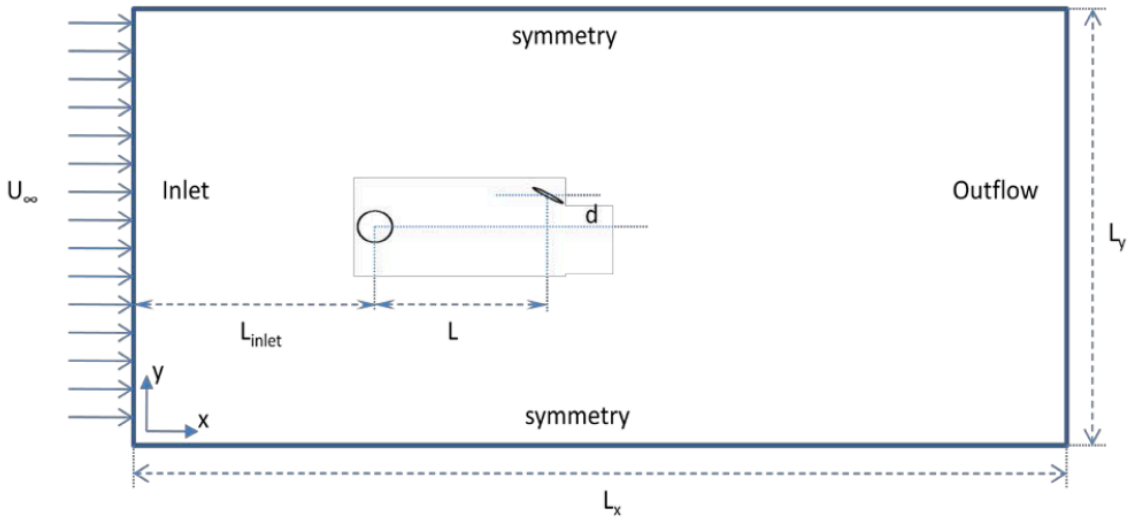

Figure 5 Sketch of the configuration for simulation and boundary conditions.

Table 1 Simulation cases

	L=3m			*L*=5m			*L*=10m		
	d=-1m	*d*=0m	*d*=1m	*d*=-1m	*d*=0m	*d*=1m	*d*=-1m	*d*=0m	*d*=1m
0°		Case 1			Case 6			Case11	
30°	Case 2	Case 3	Case 4	Case 7	Case 8	Case 9	Case12	Case13	Case14
45°		Case 5			Case10			Case15	

ANSYS 15[42] is used to simulate these two-dimensional, uniform flow cases. The unstructured mesh is used for the entire simulation domain. There are 180 nodes for both cylinder and airfoil. The maximum mesh size for boundaries is 0.5*D*.

3.2 Validation Simulation Results

In this section, the validation results and comparison with Liao et al. are carried out in three parts: the effects of incident angle, the effects of longitudinal spacing, and the force characteristics.

3.2.1 Effects of Incident Angle

Figure 6 shows the lift and drag coefficients acting on the cylinder at *d*=0, *L*=5, and 30° incident angle, where (a) is the validation results and (b) is Liao et al.'s results. Both lift and drag coefficient reach the quasi-period after *t*=20*s*. Since the upstream cylinder is symmetrical, the time-averaged lift is 0. A comparison of Figure 6(a) and (b) shows that the validation results closely align with Liao et al.'s[39] results.

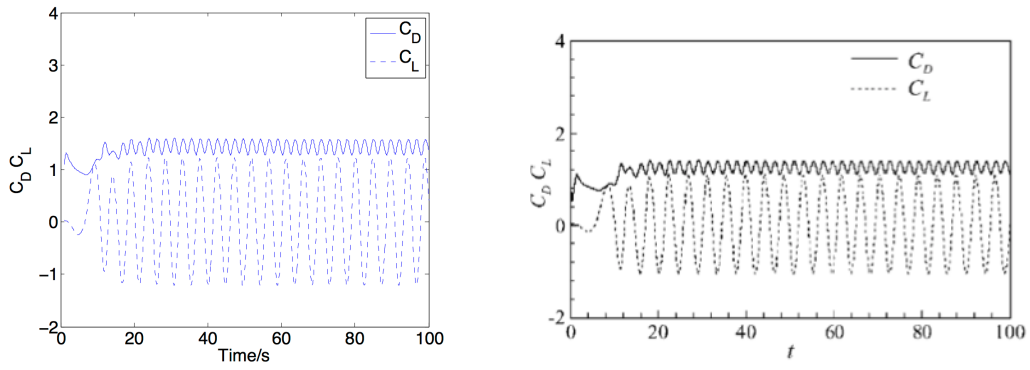

(a) (b)

Figure 6 Lift and drag coefficient history acting on the cylinder at d=0, L=5, and α=30 °: (a) validation results, (b) Liao et al.'s results.

Figure 7, Figure 8, and Figure 9 show the time-dependent lift and drag coefficient results acting on the downstream airfoil at d=0, L=5, and incident angles ranging from 0°, 30°, and 45°, respectively. C_D C_L histories on the airfoil change periodically with time, as in previous results. A comparison of Figure 6(a), Figure 7, Figure 8(a), and Figure 9(a) shows that, with different incident angles, the vortex shedding frequency of the airfoil is still synchronized with that of the airfoil, as discovered and discussed by Liao et al.[39]. As the incident angle increases, C_D amplitude increases to reach the same amplitude with C_L. Time-averaged lift and drag coefficient distribution versus incident angles will be discussed and compared in a later section. The same trend of drag coefficient can be found in Liao et al.'s results, as shown in Figure 8(b) and Figure 9(b).

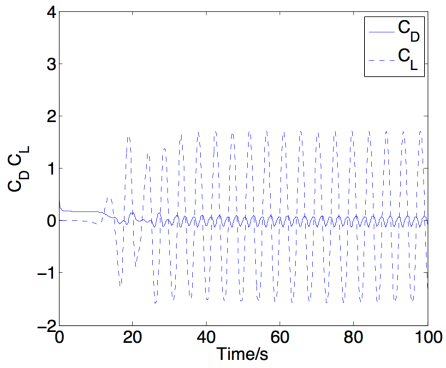

Figure 7 Lift and drag coefficient history acting on the airfoil at d=0, L=5, and α=0°.

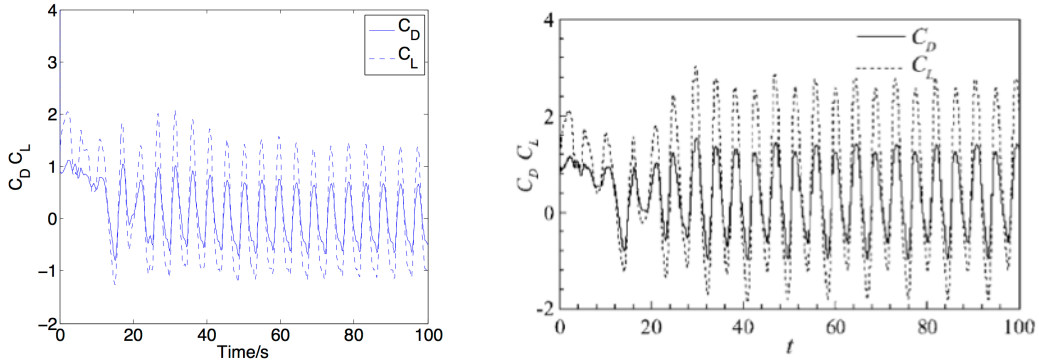

(a) (b)

Figure 8 Lift and drag coefficient history acting on the airfoil at d=0, L=5, and α=30°.

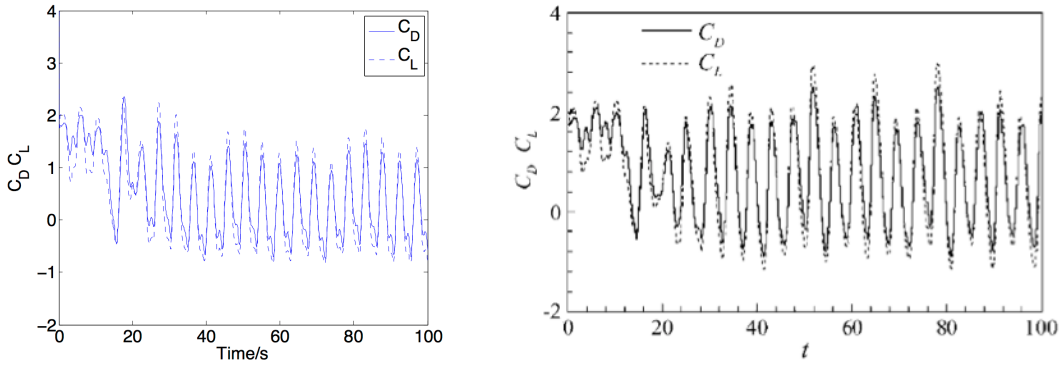

(a) (b)

Figure 9 Lift and drag coefficient history acting on the airfoil at d=0, L=5, and α=45°.

3.2.2 Effects of Longitudinal Space

The longitudinal spacing is L=3, 5, and 10, while that simulated by Liao et al. is L=3, 5, and 8.

The C_D and C_L histories of the upstream cylinder are shown in Figure 10. The results of time-dependent lift and drag coefficient acting on the airfoil at d=0, 30° incident angle with L=3, 5, and 10 is shown in Figure 11, Figure 12, and Figure 13, respectively.

The spectrum analyses of Figure 10(a) and Figure 11(a), Figure 10(b) and Figure 13(a) show that the vortex shedding frequencies of the airfoil are synchronized with that of the cylinders for L=3 and 8, respectively. Liao et al. achieved the same results.

A comparison of (a) and (b) in Figure 11 to Figure 13 shows that the results in Figure 7(a) have the same periods with the results in Figure 7(b). Also, as the spacing ratio increases, the lift, and drag coefficient histories take longer to reach quasi-sinusoidal periods, which Liao et al. [39] also discussed.

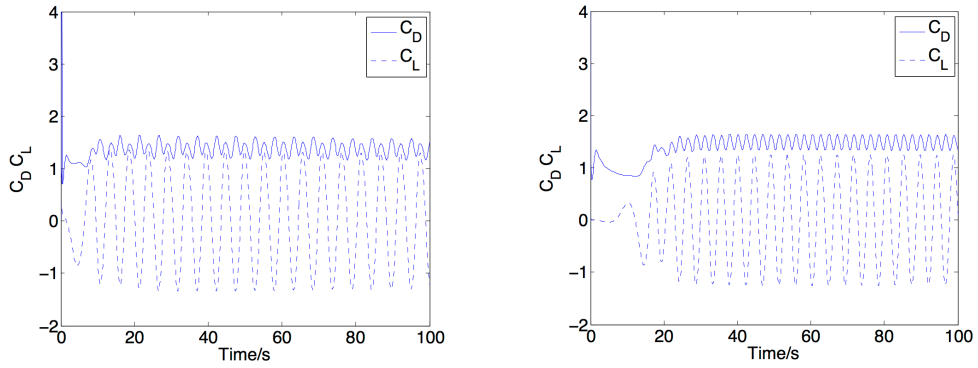

Figure 10 Lift and drag coefficient acting on cylinder at d=0, α=30°, and (a) L=3, (b) L=10.

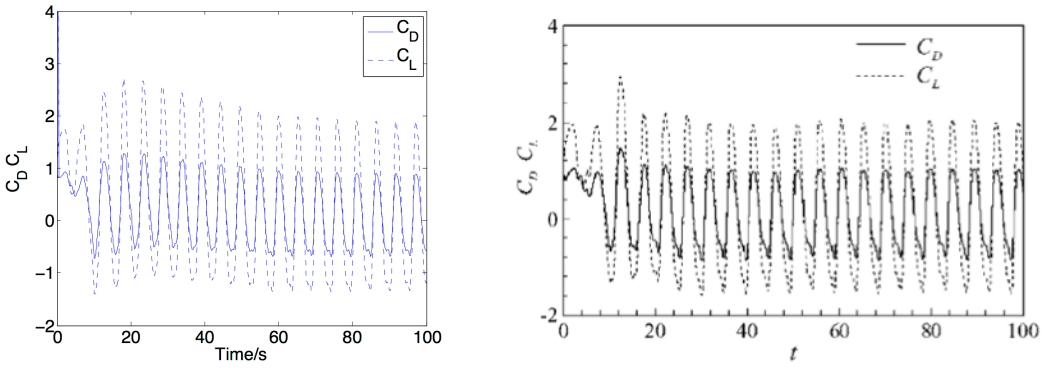

(a) (b)

Figure 11 Lift and drag coefficient history acting on the airfoil at d=0, L=3, and α=30°.

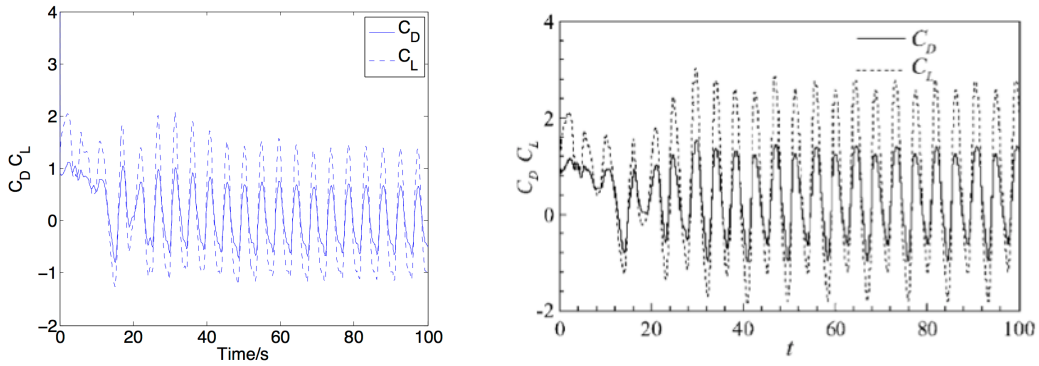

(a) (b)

Figure 12 Lift and drag coefficient acting on airfoil at d=0, L=5, and α=30°.

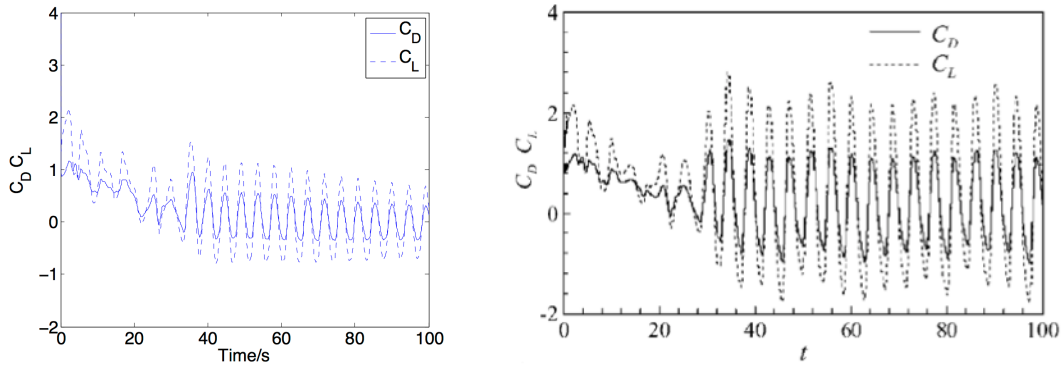

(a) (b)

Figure 13 Lift and drag coefficient acting on airfoil at d=0, (a) L=10 and (b) L=8, and α=30°.

3.2.3 Forces Characteristic

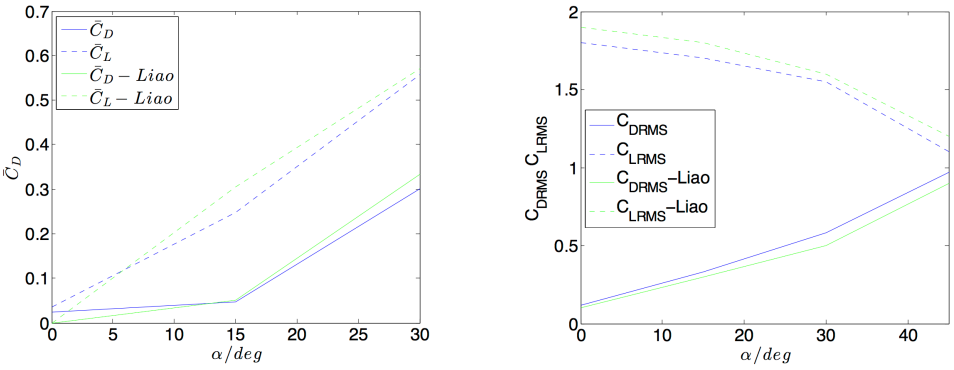

(a) (b)

Figure 14 Distribution of time-averaged C_D, C_L (a) and square mean root averaged C_D, C_L (b) versus incident angle at L=5, d=0.

Figure 14 shows the distribution of time-averaged C_D C_L and C_{DRMS} C_{LRMS} versus incident angles at L=5, d=0. As the incident angle increases, the averaged C_D, C_L, C_{DRMS} increases and C_{LRMS} decreases. As the airfoil shape is symmetrical in the simulations, the square mean root drag and lift coefficients approach together at a 45° angle of attack. As shown in Figure 14, when the incident angle is smaller than 45°, both averaged C_L and C_{LRMS} have larger values with respect to averaged C_D and C_{DRMS} for the same incident angle. The same results were discussed in Liao et al.'s[39] paper.

Therefore, the numerical strategy used in this study has been verified: the numerical solutions are reliable.

4 RESULTS AND DISCUSSION

4.1Tandem-cylinders/Cylinder-airfoil Configuration

4.1.1Effects of Reynolds Number

Figure 16, Figure 17, and Figure 18 show the life coefficient histories of the airfoil in cylinder-airfoil configuration. The oscillating frequency and amplitude of the upstream cylinders are the same, f=4 and A=0.0625D. The variable studied is the Reynolds numbers, Re=500, 2500, and 10000. As shown in Figure 16, Figure 17, and Figure 18, the lift histories in all three cases reach time periodic status after a certain running time. The calculation of time-averaged lift and drag coefficient at each Reynolds number results in a plot that shows the relation of each Reynolds number, and averaged C_D C_L is shown in Figure 15. As the Reynolds number increases, averaged C_L increases, while C_D decreases. This indicates that there is less drag but more lift along the airfoil due to the wake of the cylinder wake.

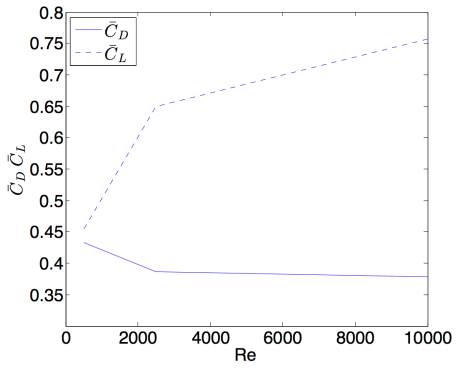

Figure 15 Time-averaged lift and drag coefficient versus Reynolds number of cylinder-airfoil configuration.

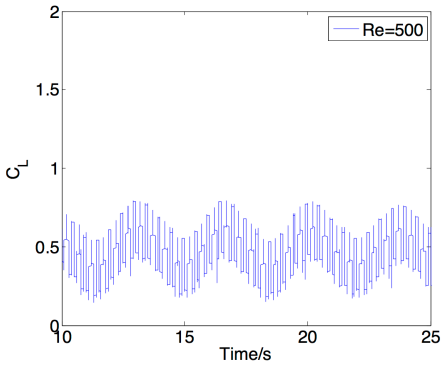

Figure 16Life coefficient history of cylinder-airfoil configurations at *Re*=500.

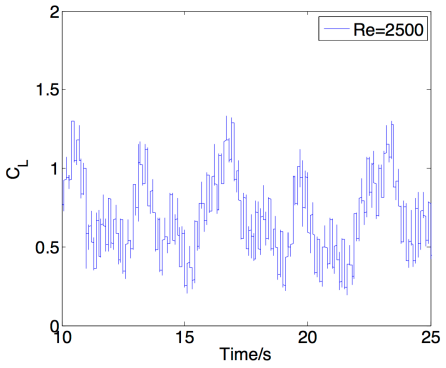

Figure 17 Lift coefficient history of cylinder-airfoil configuration at *Re*=2500.

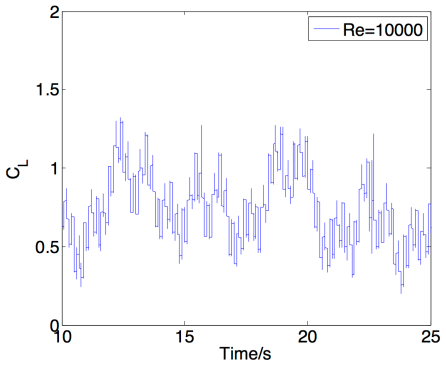

Figure 18 Lift coefficient history of cylinder-airfoil configuration at *Re*=10000.

Figure 19 shows the pressure coefficient distribution on the airfoil surface of cylinder-airfoil configurations. The C_p along the airfoil surface is plotted versus the x-axis position at different Reynolds numbers, *Re*=500, 2500, and 10000. The pressure coefficient distributions shown in Figure 19 are asymmetric due to the incident angle of the airfoil[40].

As shown in Figure 19(a), the pressure distribution on the suction surface forms a recirculating region at the trailing edge of the airfoil, which can be seen in Figure 20(b). The pressure distribution with cylinder wake on the pressure surface is much smaller than that without cylinder wake. This is due to the vortices produced by the upstream cylinder. A recirculating region occurs at the trailing edge of the airfoil without cylinder wake, while the flow attaches to the airfoil near the trailing edge with cylinder wake.

When the Reynolds number increases to 2500, the vortices produced by the upstream cylinder have less effect on the pressure surface of the airfoil. The pressure distribution on the suction surface without cylinder wakes shows that a recirculating region is formed at the half chord length, as shown in Figure 21(b). However, Figure 21(a) shows that the flow reattaches to the airfoil along the suction surface at half chord length with cylinder wake.

As the Reynolds number increases to 10000, the pressure distribution on the suction surface with cylinder wake remains almost the same as that without cylinder wake. However, a slight decrease of C_p occurs at the trailing edge with cylinder wake, which can be seen in Figure 22(a), and a recirculating region is formed.

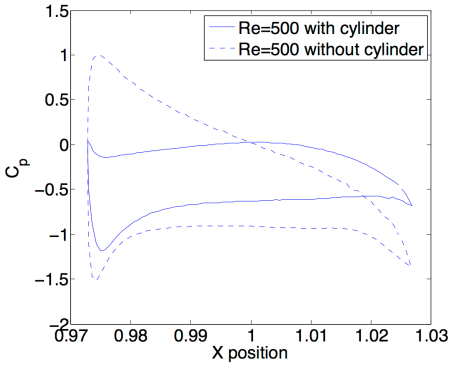

(a)

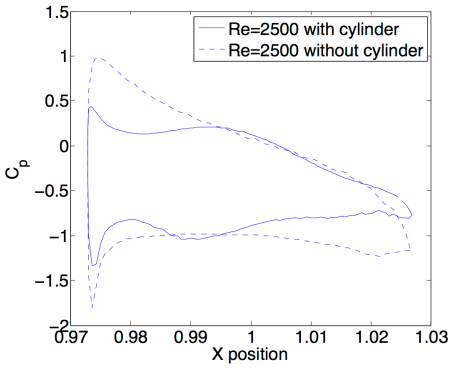

(b)

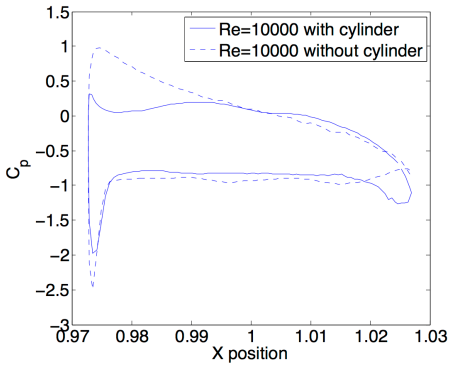

(c)

Figure 19 Pressure distribution of cylinder-airfoil configuration: (a) *Re*=500, (b) *Re*=2500, and (c) *Re*=10000.

As Reynolds increases to 2500, as shown in Figure 21, the flow separates at the leading edge in both with- and without-cylinder cases. The separation point in Figure 21(a) is slightly more delayed than that in Figure 21(b). A recirculating flow is created and reattached immediately after the flow separation with cylinder wake. A recirculating region is also formed in Figure 21(b), while the reattachment point is near the half chord length along the upper surface of the airfoil. Similarly, at *Re*=10000, the recirculating region is formed after flow separation along the upper surface of the airfoil. Therefore, the flow attaches to the airfoil and reduces the separation with cylinder wake.

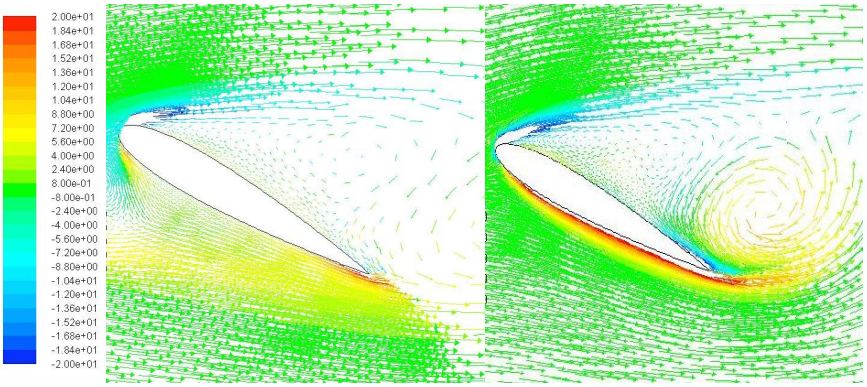

(a) (b)

Figure 20 Velocity vectors colored by vorticity of airfoil in cylinder-airfoil configuration at *Re*=500: (a) with cylinder, (b) without cylinder.

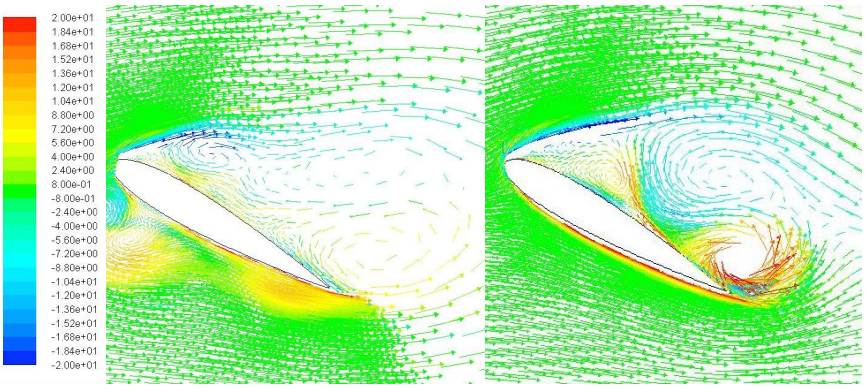

(a) (b)

Figure 21 Velocity vectors colored by vorticity of airfoil in cylinder-airfoil configuration at *Re*=2500: (a) with cylinder, (b) without cylinder.

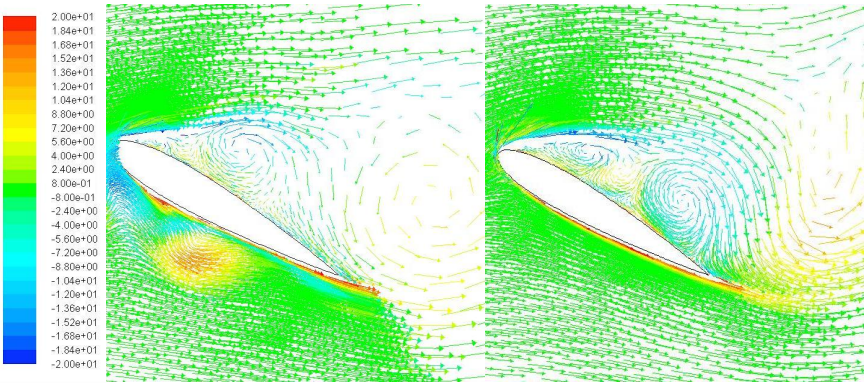

(a) (b)

Figure 22 Velocity vectors colored by vorticity of airfoil in cylinder-airfoil configuration at *Re*=10000: (a) with cylinder, (b) without cylinder.

By comparing Figure 20, Figure 21, and Figure 22, as the Reynolds number increases, more recirculating regions are formed. In addition, the recirculating region moves from the trailing edge toward the leading edge to remove the flow separation, both with and without cylinder wake. Due to the influence of the cylinder wake, the flow separation point moves slightly lower than that without cylinder wake. Also, the recirculating regions with cylinder wake are larger than those without cylinder wake, and those regions are formed near the leading edge along the whole upper surface of the airfoil.

4.1.2 Effects of Frequency

Figure 23shows velocity vectors near the surface of the rear cylinder of simulation cases for the cylinder-cylinder configuration with Re=2500, L/D=1.5. The oscillation frequency in each case is (a) 2, 0.125D (b) 4, 0.25D; and (c) 8, 0.0625D, respectively. The proportional change between the frequency and amplitude is to keep the oscillation velocity magnitude the same. The upstream cylinder diameter is 0.3D. For comparative purposes, a case of flow over a single cylinder at the same Reynolds number is simulated, and the velocity vectors are plotted in Figure 24.

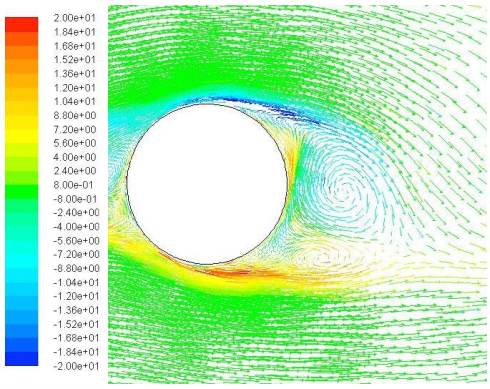

(a)

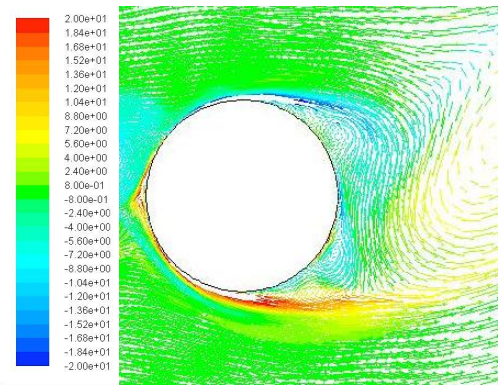

(b)

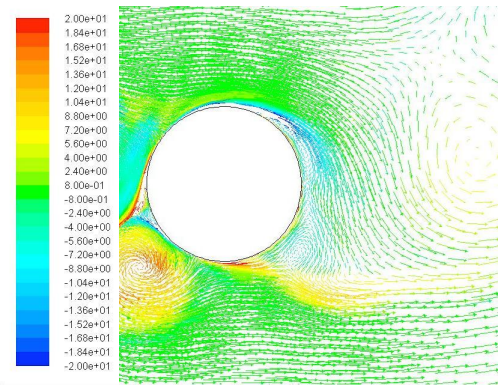

(c)

Figure 23Velocity vectors for the cases of cylinder-cylinder configuration. The color represents vorticity: (a) f=2, (b) f=4, and (c) f=8.

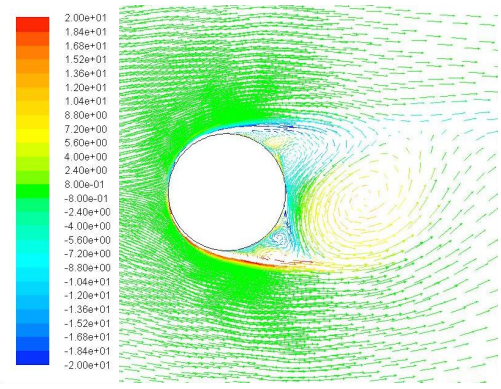

Figure 24Velocity vectors for a case of flow over a cylinder. The color represents vorticity.

A comparison of Figure 23 and Figure 24 reveals that vortex shedding in the wake of the rear cylinder is reduced in comparison to the wake of the single-cylinder case. A comparison of Figure 23(a), (b), and (c) reveals that the flow separation is reduced more when the oscillation frequency increases. Although flow separation occurs on the surface of the cylinder in all the cases in Figure 23 and Figure 24, the flow reattaches to the surface faster in the cylinder-cylinder cases by producing a smoother flow field under the influence of the vortices shed from the upstream cylinder.

Time-dependent lift coefficient histories at different oscillating frequencies of airfoil in cylinder-airfoil configurations are shown in Figure 26, Figure 27, and Figure 28. The Reynolds number, the oscillating amplitude, and the incident angle are fixed as 10000, 0.0625D, and 30°, respectively. Oscillating frequencies of the upstream cylinder are 2, 4, and 8. As shown in Figure 26, Figure 27, and Figure 28, all three cases reach periodic status.

Figure 25 shows the averaged lift and drag coefficient versus upstream cylinder oscillation frequency. As the frequency increases, lift coefficient increases, while drag coefficient decreases. This indicates that, at high oscillation frequency, the effect of the cylinder wake is stronger than at low oscillation frequency.

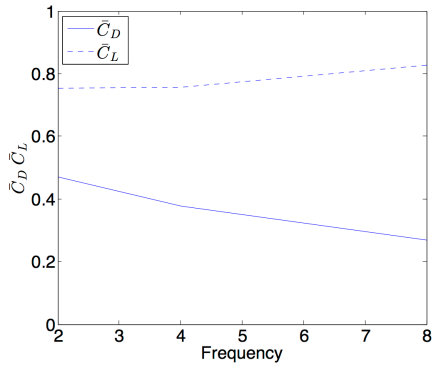

Figure 25Averaged lift and drag coefficient distribution versus cylinder oscillation frequency.

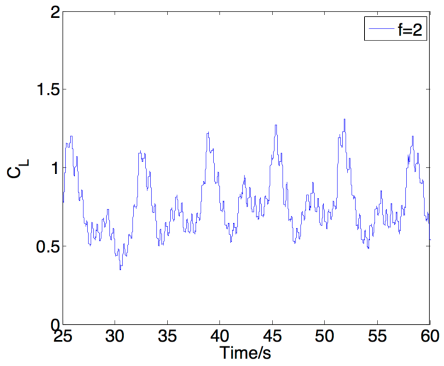

Figure 26 Lift coefficient history of cylinder-airfoil configuration at *f*=2.

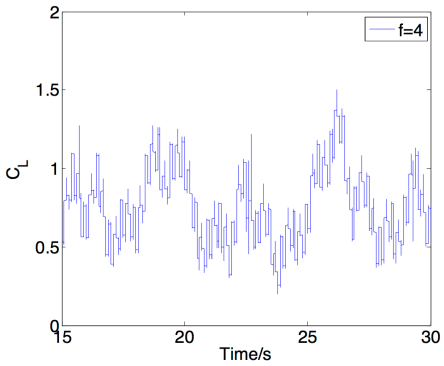

Figure 27 Lift coefficient history of cylinder-airfoil configuration at *f*=4.

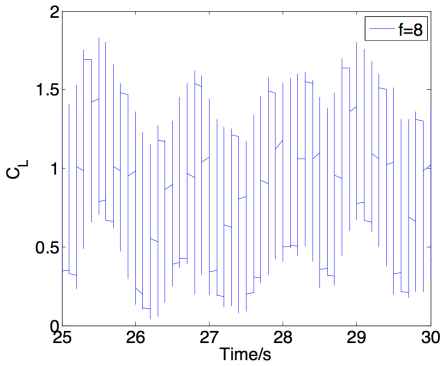

Figure 28 Lift coefficient history of cylinder-airfoil configuration at *f*=8.

The pressure distribution along the airfoil surface is shown in Figure 29. When oscillating frequency *f*=2, the pressure distribution with cylinder wake on the suction surface remains nearly the same as that without cylinder wake, in spite of a slight decrease at the trailing edge. This indicates that the cylinder wake does not significantly influence the suction surface. The slightly decreased C_p shows a recirculating region, which can be seen in Figure 30(a). As oscillating

frequency increases to 4, the vortices produced by the upstream cylinder have a larger effect than those at a lower frequency. As discussed in 4.1.1, a reattachment flow is present at the trailing edge on the suction surface.

When oscillating frequency increases to 8, the pressure distribution on the suction surface decreases much more than the distribution without cylinder wake. This indicates that the flow separation is reduced, and a reattachment flow is formed after the separation, which can be seen in Figure 31(a). At half chord length, the pressure distribution on suction surface turns to approach the distribution without cylinder wake, which can be seen in Figure 31(a) and (b); recirculating regions are formed in both cases.

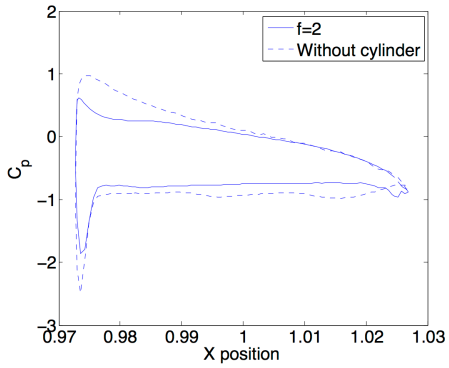

(a)

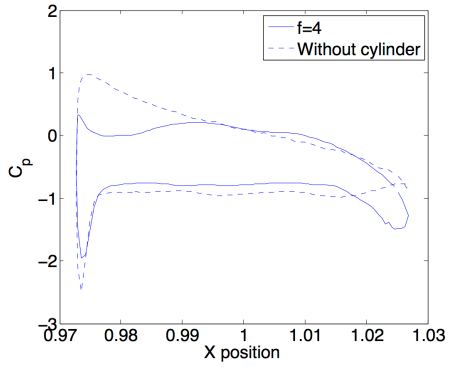

(b)

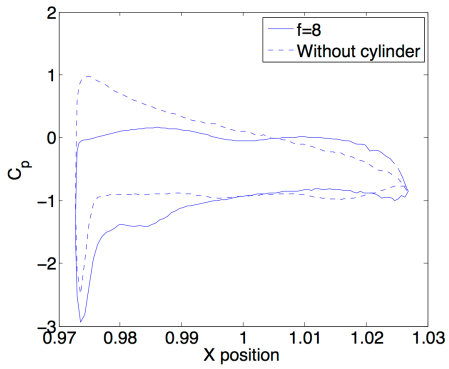

(c)

Figure 29 Pressure coefficient distribution of airfoil in cylinder-airfoil configuration: (a) *f*=2, (b) *f*=4, and (c) *f*=8.

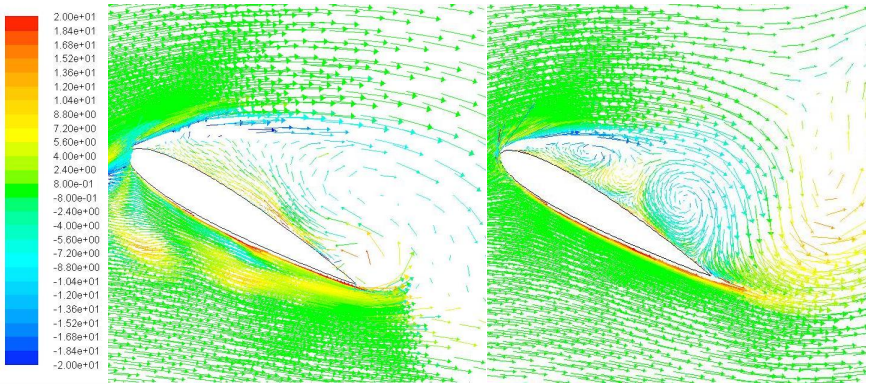

(a) (b)

Figure 30 Velocity vectors colored by vorticity of airfoil in cylinder-airfoil configuration: (a) with cylinder *f*=2, (b) without cylinder.

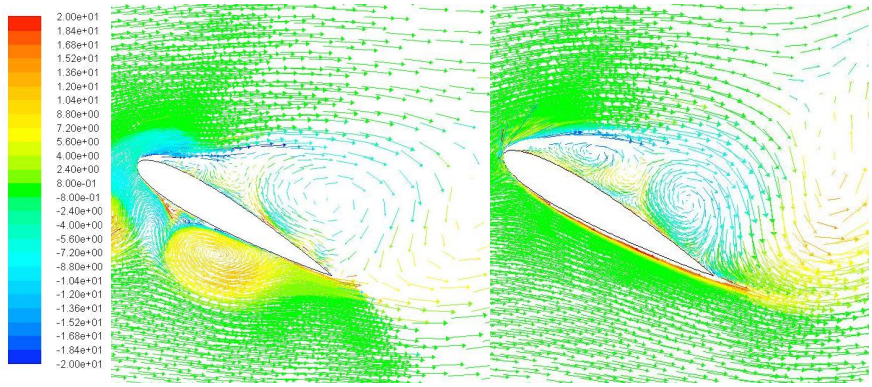

(a) (b)

Figure 31 Velocity vectors colored by vorticity of airfoil in cylinder-airfoil configuration: (a) with cylinder *f*=8, (b) without cylinder.

4.1.3 Effects of Amplitude

In order to study the effect of amplitude, in this section, the Reynolds number, oscillating frequency, and incident angle are fixed as 10000, 8, and 30°, respectively. The oscillating amplitudes are 0.25*D*, 0.125*D*, and 0.0625*D*. In Figure 33, Figure 34, and Figure 35, the time-dependent lift coefficient histories are plotted at different amplitudes. Each case shows a time periodic status in the time interval. The time-averaged C_D C_L versus amplitude is shown in Figure 32. As the amplitude increases, C_L decreases, and C_D increases slightly. This indicates that higher amplitude may reduce the lift and result in drag increase.

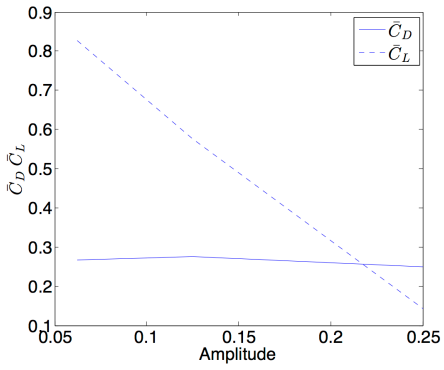

Figure 32 Time-averaged lift and drag coefficient versus amplitude of cylinder-airfoil configuration.

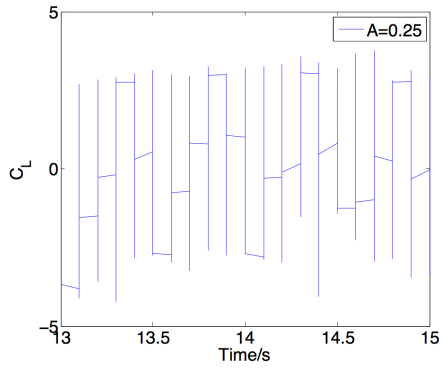

Figure 33 Lift coefficient history of cylinder-airfoil configuration of A=0.25D.

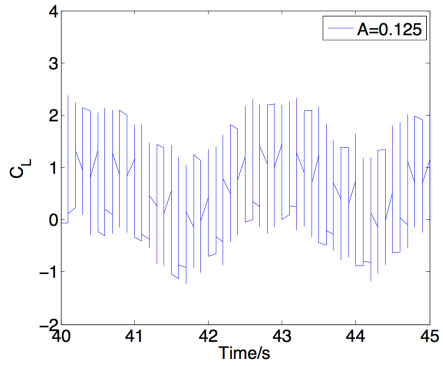

Figure 34 Lift coefficient history of cylinder-airfoil configuration of A=0.125D.

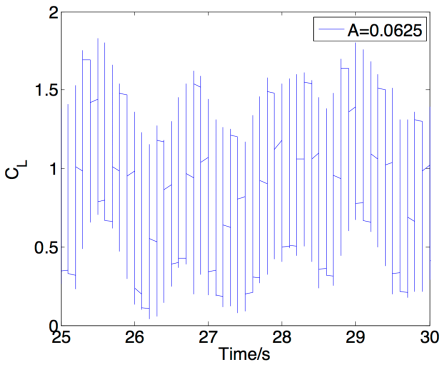

Figure 35 Lift coefficient history of cylinder-airfoil configuration of A=0.0625D.

In order to study the flow separation control effect, the pressure distribution along the airfoil surface of each case is plotted with that of single airfoil. Figure 36(a) shows the pressure distribution of an A=0.25D cylinder-airfoil configuration case. It can be seen that C_p is negative

on both surfaces of the airfoil. The distribution collapses to nearly a single line. This indicates that the lift of the airfoil is zero, but the separation is extremely strong at the leading edge. As shown in Figure 37(a), though the flow attaches to the airfoil surface well, the separation is significantly strong at the leading edge, which is due to strong vortices produced by the high-oscillating amplitude cylinder.

When amplitude reduces, as shown in Figure 36(b), the pressure distribution on lower and upper surfaces increases, yet remains negative. As shown in Figure 38(a), the flow separates strongly at the leading edge, and then a recirculating region is formed. However, at some certain time, the flow separation is removed by the vortices produced by the cylinder. However, the wake will then lead to stronger separation.

The pressure distribution at A=0.0625D was discussed in the previous section, that the flow separation is reduced at the leading edge, and then reattachment flow is formed at half chord length along the airfoil.

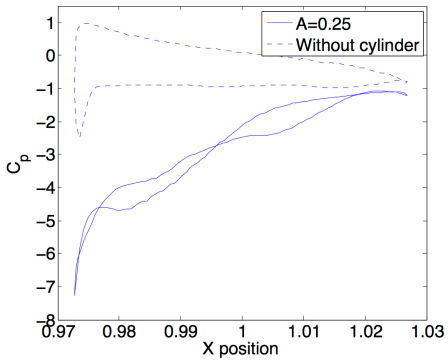

(a)

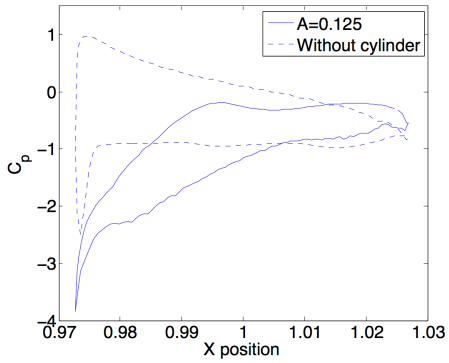

(b)

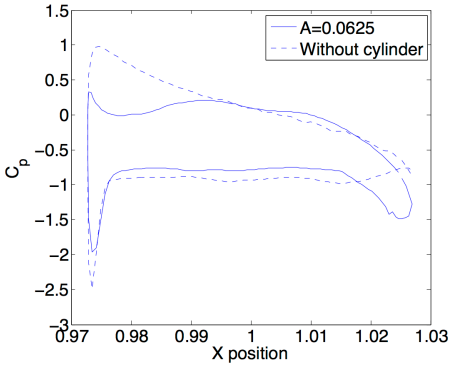

(c)

Figure 36 Pressure coefficient distribution of cylinder-airfoil configuration: (a) A=0.25D, (b) A=0.125D, and (c) A=0.0625D.

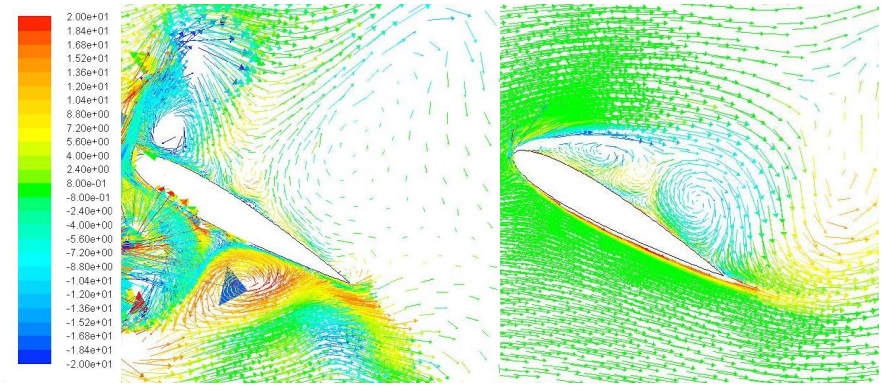

(a) (b)

Figure 37 Velocity vectors colored by vorticity of airfoil in cylinder-airfoil configuration: (a) with cylinder, A=0.25D, (b) without cylinder.

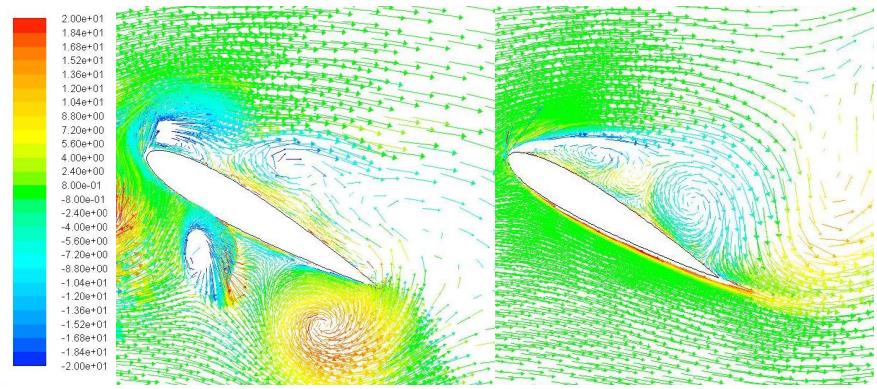

(a) (b)

Figure 38 Velocity vectors colored by vorticity of airfoil in cylinder-airfoil configuration: (a) with cylinder, A=0.125D, (b) without cylinder.

4.1.4 Effects of Incident Angle

In this section, the Reynolds number, oscillating frequency, and amplitude are fixed as 10000, 8, and 0.0625D, respectively. The incident angles that will be studied are 0°, 15°, and 30°.

Figure 40, Figure 41, and Figure 42 show the time-dependent lift coefficient histories at different angles of attack. All of them reach the time periodic status. Time-averaged lift and drag versus incident angle are shown in Figure 39. As the incident angle increases, both averaged C_D and C_L increase. No significant stall shows due to the upstream cylinder wake. The same results were reported in Liao et al.'s[39] and Takagi et al.'s[40] studies.

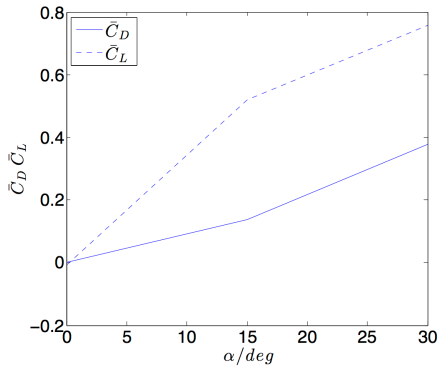

Figure 39 Time-averaged lift and drag coefficient versus incident angle of cylinder-airfoil configuration.

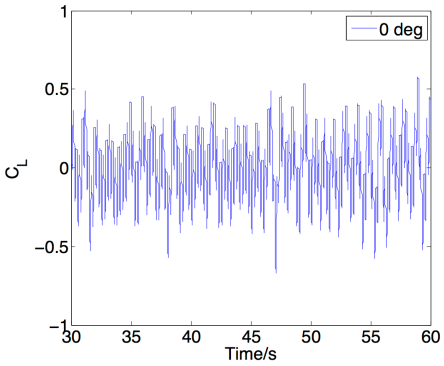

Figure 40 Lift coefficient history of cylinder-airfoil configuration of 0° incident angle.

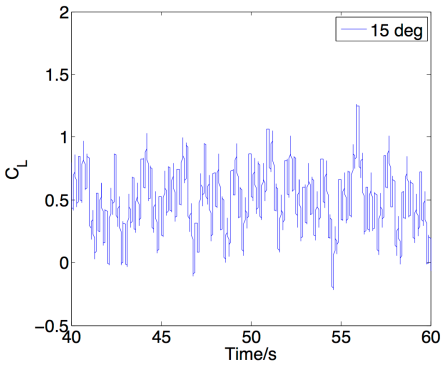

Figure 41 Lift coefficient history of cylinder-airfoil configuration of 15° incident angle.

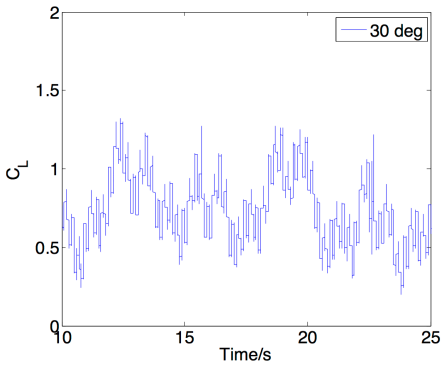

Figure 42 Lift coefficient history of cylinder-airfoil configuration of 30° incident angle.

The pressure distribution is shown in Figure 43. At a 0° angle of attack, the pressure distribution without cylinder wake collapses on a single curve due to the symmetrical configuration of the flow around the airfoil. As shown in Figure 44(b), the flow separates on both sides of the airfoil near the trailing edge, while Figure 44(a) shows that the flow attaches to the airfoil surface due to the wake of the cylinder.

Figure 45 shows the velocity vectors colored by vorticity at a 15° angle of attack. The flow separation is reduced due to the cylinder wake, as shown in Figure 45(a) and Figure 43(b). The pressure distribution on the suction surface is lower than the distribution without cylinder wake, which indicates that the flow reattaches to the surface after separation.

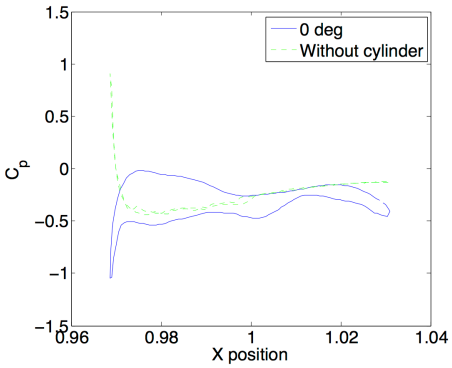

(a)

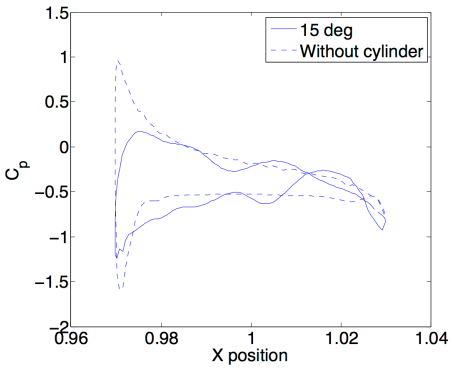

(b)

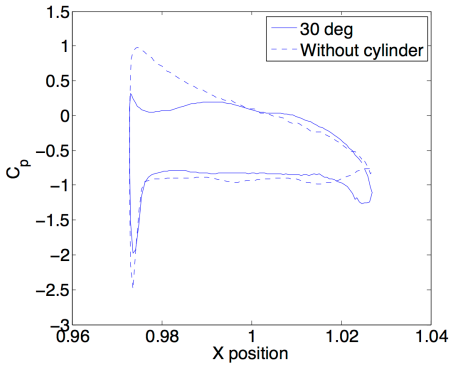

(c)

Figure 43 Pressure distribution on airfoil on cylinder-airfoil configuration: (a) 0°, (b) 15°, and (c) 30°.

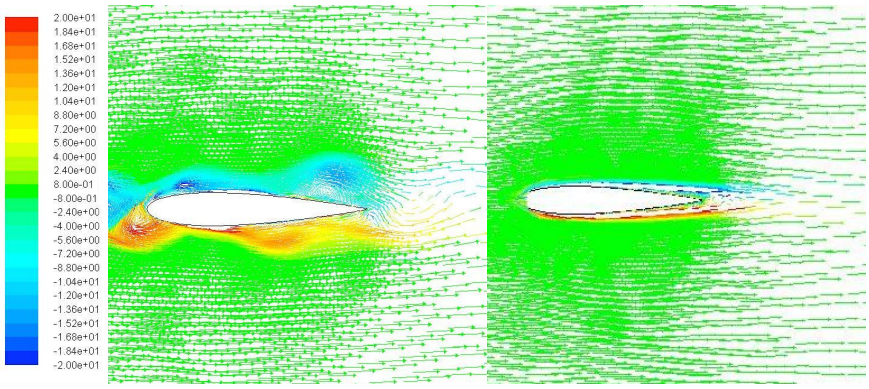

(a) (b)

Figure 44 Velocity vectors colored by vorticity at 0° angle of attack: (a) with cylinder, (b) without cylinder.

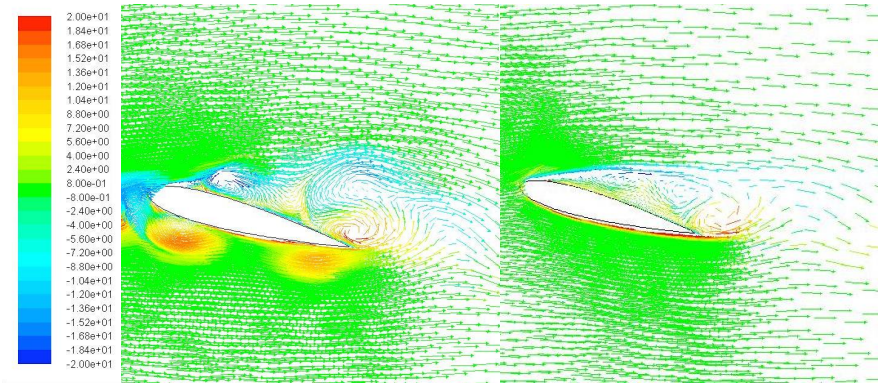

(a) (b)

Figure 45 Velocity vectors colored by vorticity at 15° angle of attack: (a) with cylinder, (b) without cylinder.

5 CONCLUSION

This study shows how the Reynolds number, the upstream cylinder's oscillating frequency, amplitude, and the incident angle of the airfoil affect the flow separation. This study was carried out by fixing one or more parameters in the simulation to understand the influence of each parameter.

By fixing the cylinder oscillation motion and incident angle, at a low Reynolds number, the flow around the airfoil is influenced mildly by the cylinder wake. No significant reduced separation can be observed on the airfoil surface. At a high Reynolds number, the separation is reduced, and a reattached flow is distinguishable at half chord length.

At certain Reynolds numbers, the upstream cylinder's motion affects the flow around the airfoil more significantly than at other Reynolds numbers. As the oscillating frequency increases, the cylinder produces more vortices. As a result, the downstream objects' separation is reduced more effectively at high frequency. Conversely, high oscillating amplitude causes strong separation near the leading edge. Therefore, a high-frequency, low-amplitude oscillating upstream object will contribute to reducing the flow separation.

The incident angle of airfoil itself also affects the separation on its surface. The separation point moves toward the leading edge as the incident angle increases. When presenting an oscillating cylinder in the upstream of the airfoil, the separation point is slightly moved backward even at zero angles of attack. Furthermore, the critical angle is increased due to the influence of the cylinder wake.

References

1. Borazjani, I., & Sotiropoulos, F. (2009). Vortex-induced vibrations of two cylinders in tandem arrangement in the proximity–wake interference region. *Journal of Fluid Mechanics*, 621, 321–364.
2. Papaioannou, G. V., Yue, D. K. P., Triantafyllou, M. S., & Karniadakis, G. E. (2008). On the effect of spacing on the vortex-induced vibrations of two tandem cylinders. *Journal of Fluids and Structures*, 24(6), 833–854.
3. Lai, W. C., Zhou, Y., So, R., & Wang, T. (2003). Interference between stationary and vibrating cylinder wakes. *Physics of fluids*, 15(6), 1687–1695.
4. Tu, J., Zhou, D., Bao, Y., Ma, J., Lu, J., & Han, Z. (2015). Flow-induced vibrations of two circular cylinders in tandem with shear flow at low Reynolds number. *Journal of Fluids and Structures*, 59, 224–251.
5. Gu, Z., & Sun, T. (1999). On interference between two circular cylinders in staggered arrangement at high subcritical Reynolds numbers. *Journal of Wind Engineering and Industrial Aerodynamics*, 80(3), 287–309.
6. Igarashi, T. (1981). Characteristics of the flow around two circular cylinders arranged in tandem: 1st report. *Bulletin of JSME*, 24(188), 323–331.
7. Kang, S. (2003). Characteristics of flow over two circular cylinders in a side-by-side arrangement at low Reynolds numbers. *Physics of Fluids (1994-present)*, 15(9), 2486–2498.
8. Dalton, C., Xu, Y., & Owen, J. C. (2001). The suppression of lift on a circular cylinder due to vortex shedding at moderate Reynolds numbers. *Journal of Fluids and Structures*, 15(3), 617–628.

9. Xu, S. J., Zhou, Y., & So, R. M. C. (2003). Reynolds number effects on the flow structure behind two side-by-side cylinders. *Physics of Fluids (1994-present)*, 15(5), 1214–1219.
10. Zhou, Y., Zhang, H. J., & Yiu, M. W. (2002). The turbulent wake of two side-by-side circular cylinders. *Journal of Fluid Mechanics*, 458, 303–332.
11. Sumner, D., Price, S. J., & Paidoussis, M. P. (2000). Flow-pattern identification for two staggered circular cylinders in cross-flow. *Journal of Fluid Mechanics*, 411, 263–303.
12. Keser, H. I., & Ünal, M. F. (2003). Flow around a circular cylinder downstream of a blunt-based flat plate in tandem and staggered arrangements. *Journal of Fluids and Structures*, 17(6), 783–791.
13. Zhou, Y., Wang, Z. J., So, R. M. C., Xu, S. J., & Jin, W. (2001). Free vibrations of two side-by-side cylinders in a cross-flow. *Journal of Fluid Mechanics*, 443, 197–229.
14. Lin, J. C., Yang, Y., & Rockwell, D. (2002). Flow past two cylinders in tandem: Instantaneous and averaged flow structure. *Journal of Fluids and Structures*, 16(8), 1059–1071.
15. Deng, J., Ren, A. L., Zou, J. F., & Shao, X. M. (2006). Three-dimensional flow around two circular cylinders in tandem arrangement. *Fluid Dynamics Research*, 38(6), 386–404.
16. Meneghini, J. R., Saltara, F., Siqueira, C. L. R., & Ferrari, J. A. (2001). Numerical simulation of flow interference between two circular cylinders in tandem and side-by-side arrangements. *Journal of Fluids and Structures*, 15(2), 327–350.
17. Kitagawa, T., & Ohta, H. (2008). Numerical investigation on flow around circular cylinders in tandem arrangement at a subcritical Reynolds number. *Journal of Fluids and Structures*, 24(5), 680–699.

18. Carmo, B. S., & Meneghini, J. R. (2006). Numerical investigation of the flow around two circular cylinders in tandem. *Journal of Fluids and Structures*, 22(6), 979–988.

19. Mahir, N., & Rockwell, D. (1996). Vortex formation from a forced system of two cylinders. Part I: Tandem arrangement. *Journal of Fluids and Structures*, 10(5), 473–489.

20. Yang, X., & Zheng, Z. C. (2010). Nonlinear spacing and frequency effects of an oscillating cylinder in the wake of a stationary cylinder. *Physics of Fluids (1994-present)*, 22(4), 043601.

21. Li, J., Chambarel, A., Donneaud, M., & Martin, R. (1991). Numerical study of laminar flow past one and two circular cylinders. *Computers & fluids*, 19(2), 155-170.

22. Sharman, B., Lien, F. S., Davidson, L., & Norberg, C. (2005). Numerical predictions of low Reynolds number flows over two tandem circular cylinders. *International Journal for Numerical Methods in Fluids*, 47(5), 423-447.

23. Bao, Y., Zhou, D., & Tu, J. (2011). Flow interference between a stationary cylinder and an elastically mounted cylinder arranged in proximity. *Journal of Fluids and Structures*, 27(8), 1425–1446.

24. Zdravkovich, M. M. (1987). The effects of interference between circular cylinders in cross flow†† An earlier version as originally presented as an invited paper, entitled “Forces on pipe clusters”, at the International Symposium on Separated Flow around Marine Structures, Norwegian Institute of Technology, Trondheim, Norway, 26–28 June 1985. *Journal of Fluids and Structures*, 1(2), 239–261.

25. Toebes, G. H. (1969). The unsteady flow and wake near an oscillating cylinder. *Journal of Basic Engineering*, 91(3), 493–502.

26. Griffin, O. M. (1971). The unsteady wake of an oscillating cylinder at low Reynolds number. *Journal of Applied Mechanics*, 38(4), 729–738.
27. Tanida, Y., Okajima, A., & Watanabe, Y. (1973). Stability of a circular cylinder oscillating in uniform flow or in a wake. *Journal of Fluid Mechanics*, 61(04), 769–784.
28. Griffin, O. M., & Ramberg, S. E. (1976). Vortex shedding from a cylinder vibrating in line with an incident uniform flow. *Journal of Fluid Mechanics*, 75(2), 257–271.
29. King, R. (1977). A review of vortex shedding research and its application. *Ocean Engineering*, 4(3), 141–171.
30. Durgin, W. W., March, P. A., & Lefebvre, P. J. (1980). Lower mode response of circular cylinders in cross-flow. *Journal of Fluids Engineering*, 102(2), 183–189.
31. Williamson, C. H. K., & Roshko, A. (1988). Vortex formation in the wake of an oscillating cylinder. *Journal of Fluids and Structures*, 2(4), 355–381.
32. Olinger, D. J., & Sreenivasan, K. R. (1988). Nonlinear dynamics of the wake of an oscillating cylinder. *Physical Review Letters*, 60(9), 797.
33. Ongoren, A., & Rockwell, D. (1988). Flow structure from an oscillating cylinder Part 1. Mechanisms of phase shift and recovery in the near wake. *Journal of Fluid Mechanics*, 191, 197–223.
34. Mittal, S., & Kumar, V. (2001). Flow-induced oscillations of two cylinders in tandem and staggered arrangements. *Journal of Fluids and Structures*, 15(5), 717–736.
35. Blackburn, H. M., & Henderson, R. D. (1999). A study of two-dimensional flow past an oscillating cylinder. *Journal of Fluid Mechanics*, 385, 255–286.

36. Sturm, H., Dumstorff, G., Busche, P., Westermann, D., & Lang, W. (2012). Boundary layer separation and reattachment detection on airfoils by thermal flow sensors. *Sensors*, 12(11), 14292–14306.

37. Jiang, Y., Mao, M. L., Deng, X. G., & Liu, H. Y. (2015). Numerical investigation on body-wake flow interaction over rod–airfoil configuration. *Journal of Fluid Mechanics*, 779, 1–35.

38. Bouzaher, M. T. (2014). Numerical Study of Flow Separation Control over a NACA2415 Airfoil. *World Academy of Science, Engineering and Technology*, *International Journal of Mechanical, Aerospace*, *Industrial, Mechatronic and Manufacturing Engineering*, 8(4), 786–789.

39. Liao, Q., Dong, G. J., & Lu, X. Y. (2004). Vortex formation and force characteristics of a foil in the wake of a circular cylinder. *Journal of Fluids and Structures*, 19(4), 491–510.

40. Takagi, Y., Fujisawa, N., Nakano, T., & Nashimoto, A. (2006). Cylinder wake influence on the tonal noise and aerodynamic characteristics of a NACA0018 airfoil. *Journal of Sound and Vibration*, 297(3), 563–577.

41. Wei, Z., New, T. H., & Cui, Y. D. (2015). An experimental study on flow separation control of hydrofoils with leading-edge tubercles at low Reynolds number. *Ocean Engineering*, 108, 336–349.

42. Fluent® Users Manual, v.15.0.2, 2014.

Appendix

Matlab code

```
%Validation simulation results
%d=0 L=5 alpha=30 airfoil
figure(1);
plot(DATA5030(:,1),DATA5030(:,2),'-b'),hold on;
plot(DATA5030(:,4),DATA5030(:,5),'--b'),hold on;
xlabel('Time/s');
ylabel('C_D C_L');
legend('C_D','C_L');
axis([0 100 -2 4]);

%d=0 L=5 alpha=30 cylinder
figure(2);
plot(DATA5030cy(:,1),DATA5030cy(:,2),'-b'),hold on;
plot(DATA5030cy(:,4),DATA5030cy(:,5),'--b'),hold on;
xlabel('Time/s');
ylabel('C_D C_L');
legend('C_D','C_L');
axis([0 100 -2 4]);

%d=0 L=5 alpha=0 airfoil
figure(3)
plot(DATA500(:,1),DATA500(:,2),'-b'),hold on;
plot(DATA500(:,4),DATA500(:,5),'--b'),hold on;
xlabel('Time/s');
ylabel('C_D C_L');
legend('C_D','C_L');
axis([0 100 -2 4]);

%d=0 L=5 alpha=45 airfoil
figure(4)
plot(DATA5045(:,1),DATA5045(:,2),'-b'),hold on;
plot(DATA5045(:,4),DATA5045(:,5),'--b'),hold on;
xlabel('Time/s');
ylabel('C_D C_L');
legend('C_D','C_L');
axis([0 100 -2 4]);

%d=0 L=3 alpha=30 airfoil
figure(5)
plot(DATA3030(:,1),DATA3030(:,2),'-b'),hold on;
plot(DATA3030(:,4),DATA3030(:,5),'--b'),hold on;
xlabel('Time/s');
ylabel('C_D C_L');
legend('C_D','C_L');
axis([0 100 -2 4]);

%d=0 L=3 alpha=30 cylinder
figure(6)
plot(DATA3030cy(:,1),DATA3030cy(:,2),'-b'), hold on;
plot(DATA3030cy(:,4),DATA3030cy(:,5),'--b'),hold on;
xlabel('Time/s');
ylabel('C_D C_L');
```

```
legend('C_D','C_L');
axis([0 100 -2 4]);

%d=0 L=10 alpha=30 airfoil
figure(7)
plot(DATA10030(:,1),DATA10030(:,2),'-b'), hold on;
plot(DATA10030(:,4),DATA10030(:,5),'--b'),hold on;
xlabel('Time/s');
ylabel('C_D C_L');
legend('C_D','C_L');
axis([0 100 -2 4]);

%d=0 L=10 alpha=30 cylinder
figure(8)
plot(DATA10030cy(:,1),DATA10030cy(:,2),'-b'), hold on;
plot(DATA10030cy(:,4),DATA10030cy(:,5),'--b'),hold on;
xlabel('Time/s');
ylabel('C_D C_L');
legend('C_D','C_L');
axis([0 100 -2 4]);

%averaged C_D C_L versus incident angle of d=0, L=5
figure(9)
plot(avecdclangle(:,1),avecdclangle(:,3),'-b'),hold on;
plot(avecdclangle(:,1),avecdclangle(:,2),'--b'),hold on;
plot(avecdclangle(:,1),avecdclangle(:,5),'-g'),hold on;
plot(avecdclangle(:,1),avecdclangle(:,4),'--g'),hold on;
xlabel('$\alpha/deg$','interpreter','latex');
ylabel('$\bar{C}_D$','interpreter','latex');
h=legend('$\bar{C}_D$','$\bar{C}_L$','$\bar{C}_D-Liao$','$\bar{C}_L-Liao$',2)
;
set(h,'interpreter','latex');

%averaged rms C_D C_L versus incident angle of d=0 L=5
figure(10);
plot(rms(:,1),rms(:,6),'-b'),hold on;
plot(rms(:,1),rms(:,5),'--b'),hold on;
plot(rms(:,1),rms(:,3),'-g'),hold on;
plot(rms(:,1),rms(:,2),'--g'),hold on;
xlabel('$\alpha/deg$','interpreter','latex');
ylabel('C_D_R_M_S C_L_R_M_S');
legend('C_D_R_M_S','C_L_R_M_S','C_D_R_M_S-Liao','C_L_R_M_S-Liao');

%airfoil Reynolds number effect
%C_L histories re=500
figure(1);
plot(re500cdcl(:,4),re500cdcl(:,5),'-b'),hold on;
xlabel('Time/s');
ylabel('C_L');
legend('Re=500');
axis([10 25 0 2]);

%C_L Re=2500
figure(2);
plot(re2500cdcl(:,4),re2500cdcl(:,5),'-b'),hold on;
xlabel('Time/s');
ylabel('C_L');
```

```
legend('Re=2500');
axis([10 25 0 2]);

%C_L Re=10000
figure(3);
plot(re10000cdcl(:,4),re10000cdcl(:,5),'-b'),hold on;
xlabel('Time/s');
ylabel('C_L');
legend('Re=10000');
axis([10 25 0 2]);

%airfoil Reynolds number effect
%averaged C_D C_L vs Re
figure(4)
plot(reavecdcl(:,1),reavecdcl(:,2),'-b'),hold on;
plot(reavecdcl(:,1),reavecdcl(:,3),'--b'),hold on;
xlabel('Re')
ylabel('$\bar{C}_D$ $\bar{C}_L$','interpreter','latex');
h=legend('$\bar{C}_D$','$\bar{C}_L$',2);
set(h,'interpreter','latex');

%airfoil Reynolds number effect
%C_p distribution Re=500
figure(5)
plot(recp(:,1),recp(:,2),'-b'),hold on;
plot(recp(:,10),recp(:,11),'--b'),hold on;
xlabel('X position');
ylabel('C_p');
legend('Re=500 with cylinder','Re=500 without cylinder');
axis([0.97 1.03 -2 1.5]);

%airfoil Reynolds number effect
%C_p distribution Re=2500
figure(6)
plot(recp(:,4),recp(:,5),'-b'),hold on;
plot(recp(:,13),recp(:,14),'--b'),hold on;
xlabel('X position');
ylabel('C_p');
legend('Re=2500 with cylinder','Re=2500 without cylinder');
axis([0.97 1.03 -2 1.5]);

%airfoil Reynolds number effect
%C_p distribution Re=10000
figure(7)
plot(recp(:,7),recp(:,8),'-b'),hold on;
plot(recp(:,16),recp(:,17),'--b'),hold on;
xlabel('X position');
ylabel('C_p');
legend('Re=10000 with cylinder','Re=10000 without cylinder');
axis([0.97 1.03 -3 1.5]);



%frequency effect
%f=2 C_L
figure(1);
```

```
plot(f2cdcl(:,4),f2cdcl(:,5),'-b'), hold on;
xlabel('Time/s');
ylabel('C_L');
legend('f=2');
axis([25 60 0 2]);

%f=4 C_L
figure(2);
plot(f4cdcl(:,4),f4cdcl(:,5),'-b'), hold on;
xlabel('Time/s');
ylabel('C_L');
legend('f=4');
axis([15 30 0 2]);

%F=8
figure(3);
plot(f8cdcl(:,4),f8cdcl(:,5),'-b'), hold on;
xlabel('Time/s');
ylabel('C_L');
legend('f=8');
axis([25 30 0 2]);

%f=2 C_p
figure(4);
plot(fcp(:,1),fcp(:,2),'-b'),hold on;
plot(fcp(:,10),fcp(:,11),'--b'), hold on;
xlabel('X position');
ylabel('C_p');
legend('f=2','Without cylinder');
axis([0.97 1.03 -3 2]);

%f=4 C_p
figure(5);
plot(fcp(:,4),fcp(:,5),'-b'),hold on;
plot(fcp(:,10),fcp(:,11),'--b'), hold on;
xlabel('X position');
ylabel('C_p');
legend('f=4','Without cylinder');
axis([0.97 1.03 -3 2]);


%f=8 C_p
figure(6);
plot(fcp(:,7),fcp(:,8),'-b'),hold on;
plot(fcp(:,10),fcp(:,11),'--b'), hold on;
xlabel('X position');
ylabel('C_p');
legend('f=8','Without cylinder');
axis([0.97 1.03 -3 2]);


%average cdcl
figure(7);
plot(favecdcl(:,1),favecdcl(:,3),'-b'),hold on;
plot(favecdcl(:,1),favecdcl(:,5),'--b'),hold on;
xlabel('Frequency');
ylabel('$\bar{C}_D$ $\bar{C}_L$','interpreter','latex');
```

```
h=legend('$\bar{C}_D$','$\bar{C}_L$',2);
set(h,'interpreter','latex');
axis([2 8 0 1]);



%aifroil Effect of amplitude

%C_L history, a=0.25
figure(1);
plot(a25cdcl(:,4),a25cdcl(:,5),'-b'),hold on;
xlabel('Time/s');
ylabel('C_L');
legend('A=0.25');
axis([13 15 -5 5]);

%C_L history a=0.125
figure(2);
plot(a125cdcl(:,4),a125cdcl(:,5),'-b'),hold on;
xlabel('Time/s');
ylabel('C_L');
legend('A=0.125');
axis([40 45 -2 4]);

%C_p a=0.25
figure(3);
plot(acp(:,1),acp(:,2),'-b'), hold on;
plot(acp(:,10),acp(:,11),'--b'), hold on;
xlabel('X position');
ylabel('C_p');
legend('A=0.25','Without cylinder');
axis([0.97 1.03 -8 1.5]);

%C_p a=0.125;
figure(4);
plot(acp(:,4),acp(:,5),'-b'), hold on;
plot(acp(:,10),acp(:,11),'--b'), hold on;
xlabel('X position');
ylabel('C_p');
legend('A=0.125','Without cylinder');
axis([0.97 1.03 -4 1.5]);

%C_p a=0.625
figure(5);
plot(acp(:,7),acp(:,8),'-b'), hold on;
plot(acp(:,10),acp(:,11),'--b'), hold on;
xlabel('X position');
ylabel('C_p');
legend('A=0.0625','Without cylinder');
axis([0.97 1.03 -3 1.5]);


%averaged cdcl
figure(6);
plot(aavecdcl(:,1),aavecdcl(:,2),'-b'), hold on;
plot(aavecdcl(:,1),aavecdcl(:,3),'--b'),hold on
```

```
xlabel('Amplitude')
ylabel('$\bar{C}_D$ $\bar{C}_L$','interpreter','latex');
h=legend('$\bar{C}_D$','$\bar{C}_L$');
set(h,'interpreter','latex');



%angle effect
%0 deg C_L
figure(1);
plot(angle0cdcl(:,4),angle0cdcl(:,5),'-b'), hold on;
xlabel('Time/s');
ylabel('C_L');
h=legend('$\alpha/deg$');
set(h,'interpreter','latex');
axis([30 60 -1 1]);

%15 deg C_L
figure(2);
plot(angle15cdcl(:,4),angle15cdcl(:,5),'-b'), hold on;
xlabel('Time/s');
ylabel('C_L');
h=legend('$\alpha/deg$');
set(h,'interpreter','latex');
axis([40 60 -0.5 2]);

%C_P 0 deg
figure(3)
plot(anglecp(:,1),anglecp(:,2),'-b'), hold on;
plot(anglecp(:,10),anglecp(:,11),'--g'), hold on;
xlabel('X position');
ylabel('C_p');
legend('0 deg','Without cylinder')
axis([0.96 1.04 -1.5 1.5]);

%C_P 15 deg
figure(4)
plot(anglecp(:,4),anglecp(:,5),'-b'), hold on;
plot(anglecp(:,13),anglecp(:,14),'--b'), hold on;
xlabel('X position');
ylabel('C_p');
legend('15 deg','Without cylinder');
axis([0.96 1.04 -2 1.5]);

%C_P 30 deg
figure(5)
plot(anglecp(:,7),anglecp(:,8),'-b'), hold on;
plot(anglecp(:,16),anglecp(:,17),'--b'), hold on;
xlabel('X position');
ylabel('C_p');
legend('30 deg','Without cylinder');
axis([0.96 1.04 -3 1.5]);

%average cdcl
figure(6)
plot(angleavecdcl(:,1),angleavecdcl(:,2),'-b'), hold on;
```

```
plot(angleavecdcl(:,1),angleavecdcl(:,3),'--b'), hold on;
xlabel('$\alpha/deg$','interpreter','latex');
ylabel('$\bar{C}_D$ $\bar{C}_L$','interpreter','latex');
h=legend('$\bar{C}_D$','$\bar{C}_L$',2);
set(h,'interpreter','latex');
```